Bulletin of the Seismological Society of America. Vol. 62, No. 1, pp. 325–341. February, 1972

LONG-PERIOD BODY-WAVE PROPAGATION FROM 4° TO 13°

By Donald V. Helmberger

ABSTRACT

Numerical seismograms are computed for a compressional pulse in a layered model. The simpler models consist of a fluid layer over a fluid half-space, a fluid layer over a solid half-space, and a solid layer over a solid half-space. Restricted portions of the theoretical response for a layered model approximating the Earth are constructed. Synthetic seismograms are generated using the pressure pulse appropriate for NTS events and the long-period instrument response. The interplay between the *PL* wave, the refracted wave along the lid, and the arrival from the base of the low-velocity zone is displayed. A detailed comparison between the synthetics and observations indicates a prominent low-velocity zone with appreciable seismic absorption. Observed regional wave-shape characteristics are displayed and a reconnaissance map of lateral variations along the top of the mantle presented.

Introduction

In recent years, there have been substantial efforts made at investigating the top of the mantle and the character of the low-velocity zone (LVZ). These studies normally made use of surface-wave dispersion and short-period seismic profiling. The former suffers from poor resolving power, whereas the latter suffers from too much. That is, in most short-period profiles, in the ranges 4° to 13°, the only measurement of value is the first-arrival time since the amplitudes are usually contaminated by interferences in the crustal wave guide. Nevertheless, this method has provided invaluable information about lateral variations in Moho velocity, even though it is not clear how much of the top of the mantle is sampled in this measurement. Ideally, one would like to work with periods that are just long enough to establish amplitude stability, probably about 5 sec. However, even at much longer periods, one can see the results of lateral variations, as seen in Figure 1.

This figure contains two profiles superimposed. The location of the event, as well as the LRSM stations used in this study, is given in Figure 2. The July 5 earthquake has a vertical strike-slip mechanism with its node running between DR and RT (see Sykes, 1970). The stations with azimuths smaller than DR have their polarity changed. The line running through the recordings in Figure 1 indicates an apparent velocity of (6.5) and divides what is commonly called a *PL* wave. It is primarily confined to the crustal wave guide. The velocity of the *PL* waves appears to be roughly independent of azimuth, whereas the *P* waves which travel along the top of the mantle show marked differences between the two profiles. The interpretation made in this paper is that the crustal guide between the earthquake and the various stations does not change appreciably at these periods, whereas the LVZ does and, consequently, changes the arrival time as well as the shape of *P*. A complete recording of the event at NLAZ is given in Figure 3. In this study, we will be concerned with the *P* and *PL* waves, the first 120 secs of recording, with epicentral distances less than 13°.

The literature on *PL* waves is rather extensive starting with Oliver and Major (1960). Most of the resulting papers, Rosenbaum (1960), Phinney (1961a), Gilbert (1964), and Su and Dorman (1965), to name a few, treat the problem in terms of leaking-mode propagation. We will use generalized ray theory in this study and focus our attention on the relative amplitude of *P* to *PL*. Much of the fundamental work using this approach has been done by Pekeris *et al.* (1965) and Abramovici (1970). We will refer to these works many times throughout this study.

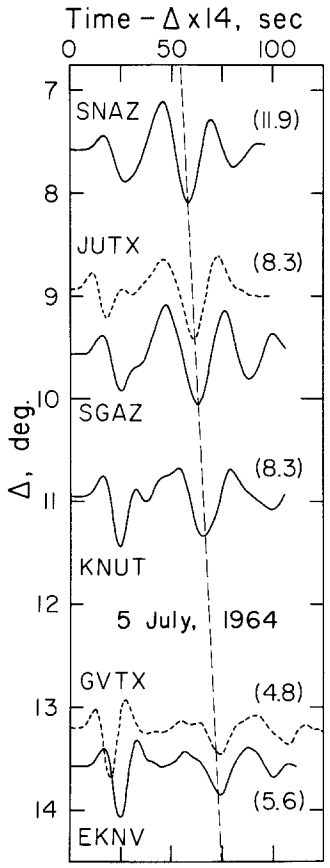

FIG. 1. Profiles of observations from the July 5, 1964 event. The numbers above the various recordings indicate the maximum amplitude of that trace.

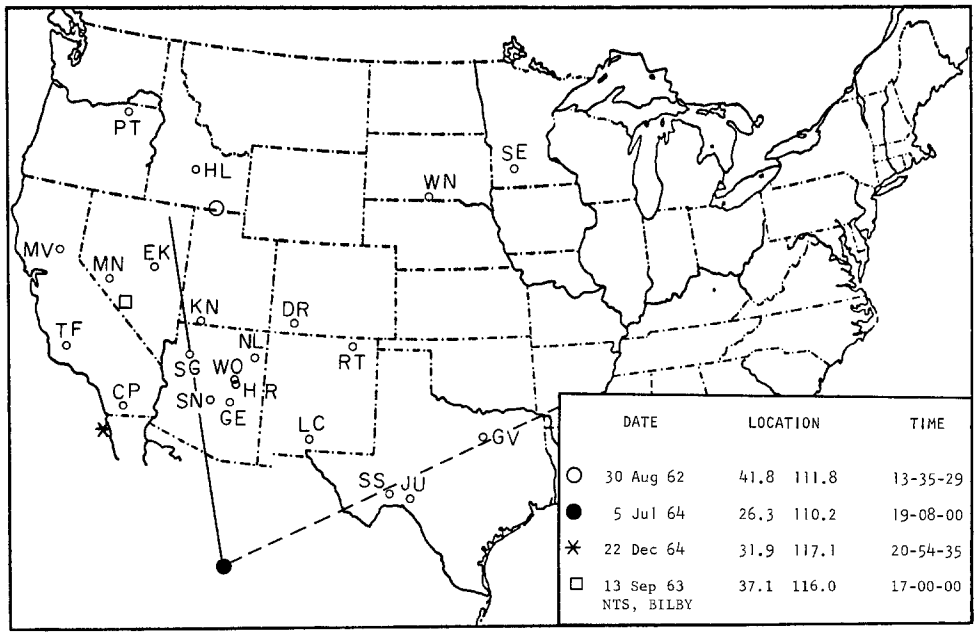

FIG. 2. LRSM recording sites and event locations.

Model Study

In this section, we review the work of Pekeris and his colleagues and demonstrate the applicability of an approximate method of generating numerical seismograms. Since our method is an order of magnitude cheaper computationally, we also discuss a number of models testing the effects of source depth and Poisson's ratio σ.

The solution of propagating elastic waves in a layered solid using exact "rays" has been given by many authors. A rather complete exposition is presented by Abramovici (1970). We use essentially the same method of series expansion except that we invert the series by applying the Cagniard-deHoop technique instead of the earlier developed Cagniard-

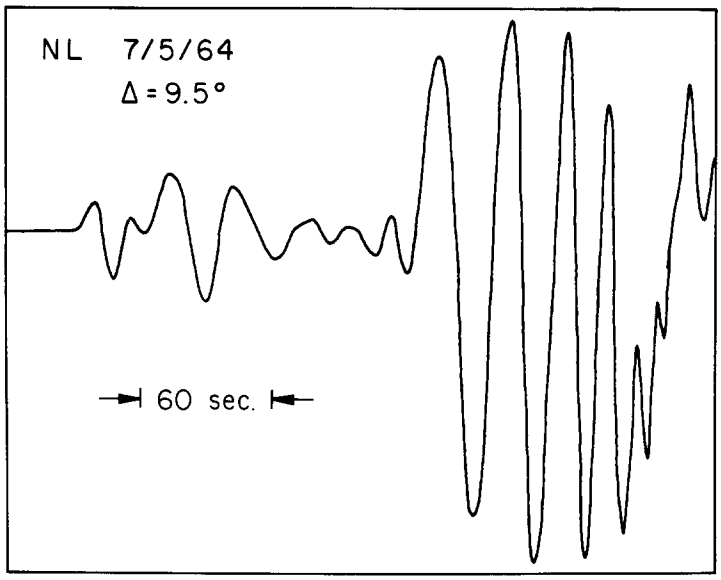

FIG. 3. Recording of the July 5, 1964 event at NL, displaying the *P*, *PL*, and Rayleigh waves, respectively.

Pekeris method. However, we do not perform the convolution operation on each ray but apply the so-called high-frequency approximation as discussed by Helmberger (1968) and Barker (1970). This approximation is equivalent to replacing the Bessel function in the radial dependence by its asymptotic form where only the first term is retained. This approximation is a very good one as pointed out by Strick (1959). Expansions out to second order for both vertical and horizontal displacements assuming *P* and *S* sources are discussed by Barker (1970).

Using the Pekeris model, solid layer of thickness H over a solid half-space, we generated the profiles presented in Figures 4 and 5. We assume Poisson's ratio $\sigma = 0.25$ or $\lambda_1 = \mu_1$ and $\mu_2 = 2\mu_1$. That is, we assumed the compressional velocities $C_1 = 1.73$ km/sec, $C_2 = 1.9$ km/sec, the shear velocities $S_1 = 1$ km/sec and $S_2 = 1.1$ km/sec, and the densities $D_1 = 1$ gm/cm^3, $D_2 = 1.65$ gm/cm^3. The *P*-pulse source has a sawtooth shape with base equal to 2Δ where Δ is equal to $0.05\ H/S_1$, unless stated otherwise. Each plot has its own amplitude scale as indicated by the *arrows*. We also applied a reduced time scale. Our S_1 is equivalent to their C so that the *top diagram* of their Figure 4 should be compared with $\rho = 5$ in our Figure 4. The agreement between the exact solutions (their Figures 4–12) and the approximate solutions (our Figures 4 and 5) is more than adequate for our purposes. The ticks labeled *P* and *PS* indicate the arrivals of the direct *P* and *PS* reflected times (see Pekeris *et al.* (1965) for a complete ray labeling

presentation). The reflection times of all multiples containing only *P*-mode crossings arrive asymptotically to the direct *P* arrival. This feature is manifested in Figure 4 by the cluster of short-period peaks following *P*. All multiples containing one *S* will have their reflected times occur asymptotically to reflected *PS*, etc. The longer-period motion in

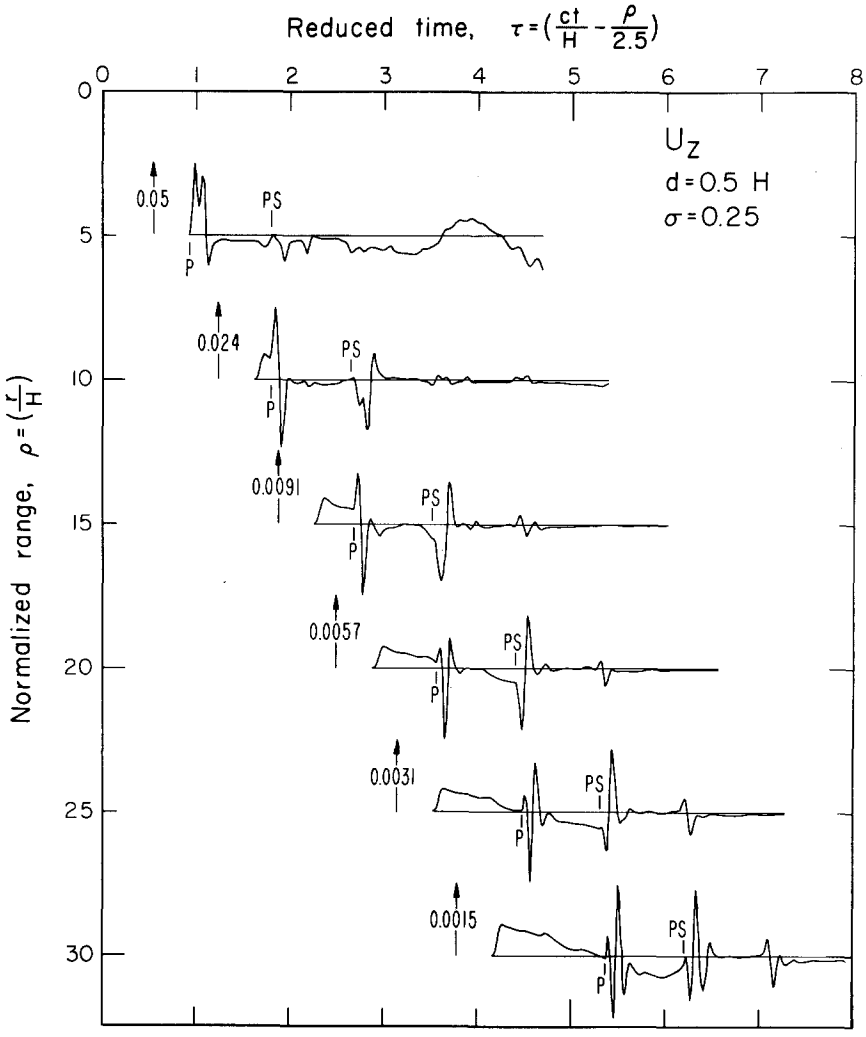

FIG. 4. Vertical displacement for a *P* pulse in a layer over a solid. The direct *P* and reflected *PS* times are indicated. Source depth, *d*, is 0.5*H*.

these responses is controlled almost entirely by refractions. The bumps following the onset are caused by reflected-refractions, for example $\rho = 30$, $\tau = 4.6$. The long-period motion starting at $\rho = 15$, $\tau = 3.3$ is caused by the *PS* refraction; that is, the generalized ray travels to the bottom as a compressional wave, along the bottom as a compressional wave and back to the surface as a shear wave. It has negative polarity. At larger ranges, multiples dominate and summation of these refractions containing at least one *S* gives rise to the long-period part of the *PL* wave. The slower-traveling reflected energy has shorter periods and thus the ray explanation of dispersion.

By moving the source, we can change the position of the critical points and shift the pattern as seen in Figures 6 and 7. The response $\rho = 20$, $H = 0.1$ of Figure 6 and $\rho = 20$,

$H = 0.9$ of Figure 7 looks like $\rho = 15$ and $\rho = 25$ in Figure 4, respectively. The interference between the multiple reflections arriving near P and PS changes markedly but we are more interested in the longer periods in this study.

By changing σ in the layer, we can drastically change the reflection coefficients and get an entirely different behavior, as can be seen in Figures 8 and 9. The numerical seismo-

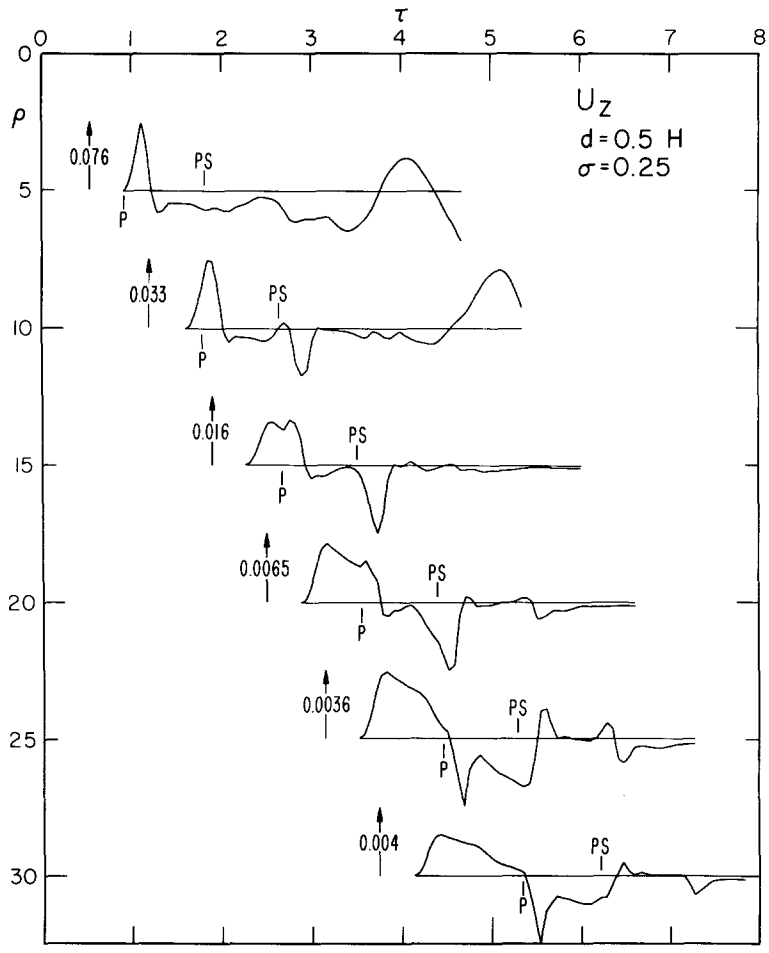

FIG 5. Vertical displacement for the same model as Figure 4 assuming $\Delta = 0.2H/S_1$.

grams for models of a fluid layer over a fluid half-space and a fluid layer over a solid half-space are given in Figures 10 and 11. The behavior displayed in Figure 10 is rather simple since the reflection coefficient at the bottom interface cannot change signs between the onset of the refraction and the reflection. Since the reflection coefficient at the surface is (-1), the reflected-refracted multiples have alternating signs and give the oscillatory appearance at $\rho = 15$ and 20. One can see the dispersive nature of the P-mode developing at $\rho = 20$. The direct P, $\tau = 3.6$, is the onset of the so-called rider wave and the rays nearest critical angle form the Airy phase as discussed in the classic papers by Pekeris (1948) and Pekeris, Longman and Lifson (19 9). In the case of a solid bottom, Figure 11, the $\bar{P}$ pole, as discussed by Gilbert and Laster (1962), distorts the refracted P waves. That is, the reflection coefficient, $R(p(t))$, changes rapidly soon after the onset. This feature is caused by the S-wave radiation out of the bottom as is well known (see

Phinney, 1961a and b). The amplitude of the multireflected rays are very strong at $\rho = 20$, which indicates that a very soft layer over a hard bottom is a good wave guide.

Increasing σ in the layer produces strong coupling between the P and S propagation and gives the recording, Figure 8, a short-period ringing nature with little indication of PL development. As the layer becomes very hard, Figure 9 with $\sigma = 0.15$, the shear contrast at the bottom decreases and the P waves dominate.

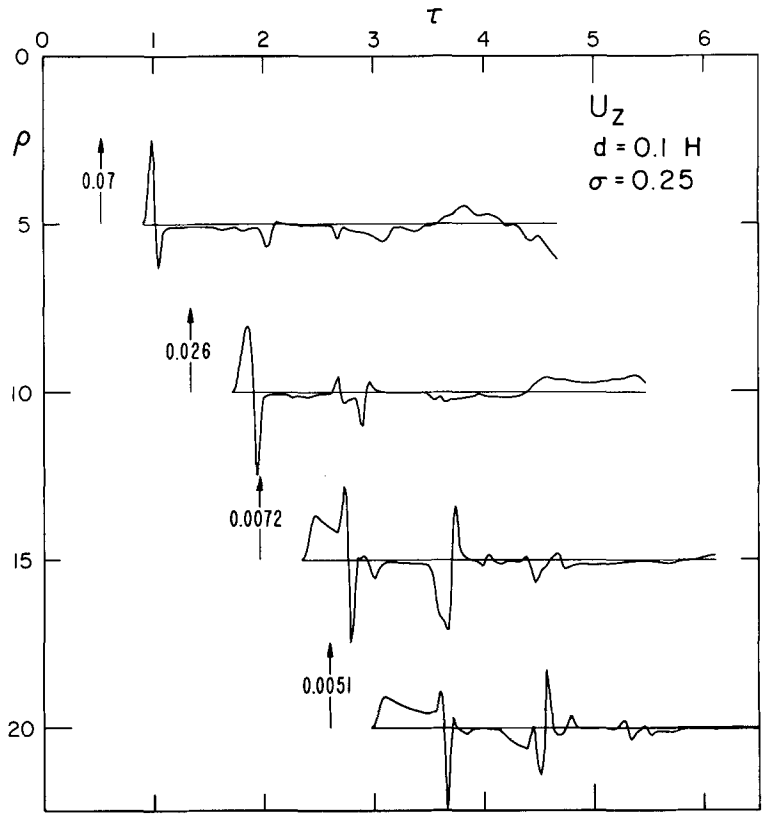

FIG. 6. Vertical displacement for the source situated near the surface.

Thus we conclude that models containing fluids have very little to do with the types of PL waves discussed in this paper. It would also appear that the conditions for PL wave support require fairly delicate boundary conditions. It is unlikely that we will see long-period PL waves on recordings taken on the moon, since we are probably dealing with a soft layer over a hard half-space (see Figure 8).

SYNTHETIC SEISMOGRAMS

We present here some synthetic seismograms based on relatively simple models. The crust is considered to be a single layer over a half-space for modeling the PL wave. A partial justification for this assumption can be obtained by examining the ray paths for a more realistic model. The rays approaching the surface are deflected toward the vertical by the decrease in velocity. For short-enough wavelengths and a very low-velocity surface layer, the effective reflection coefficient can be (-1). The multiple reflections in such a layer produce an oscillatory behavior (for example, see Gilbert and Helmberger,

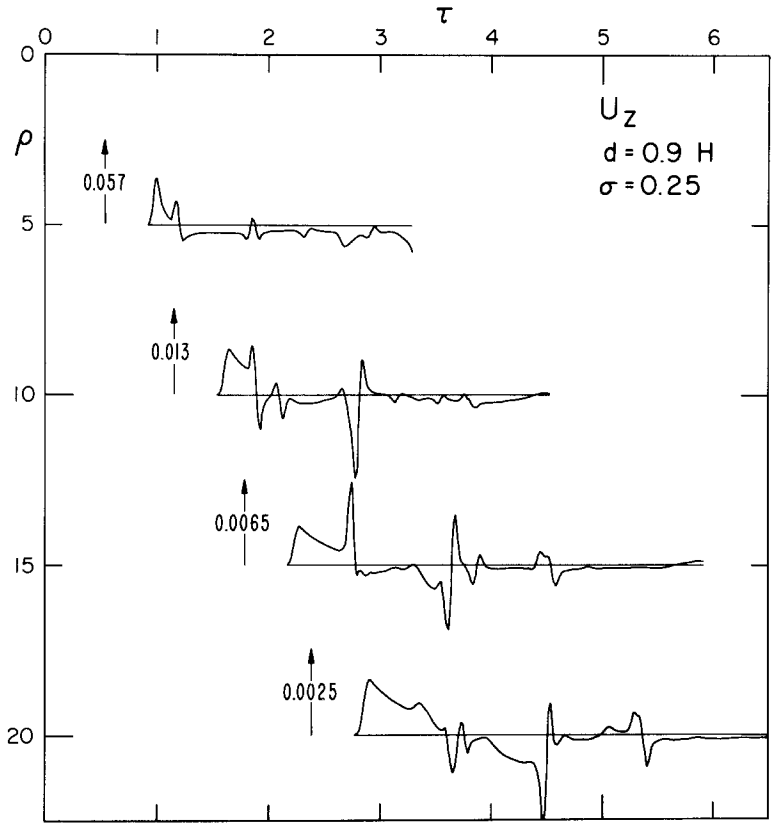

FIG. 7. Vertical displacement for the source situated near the bottom.

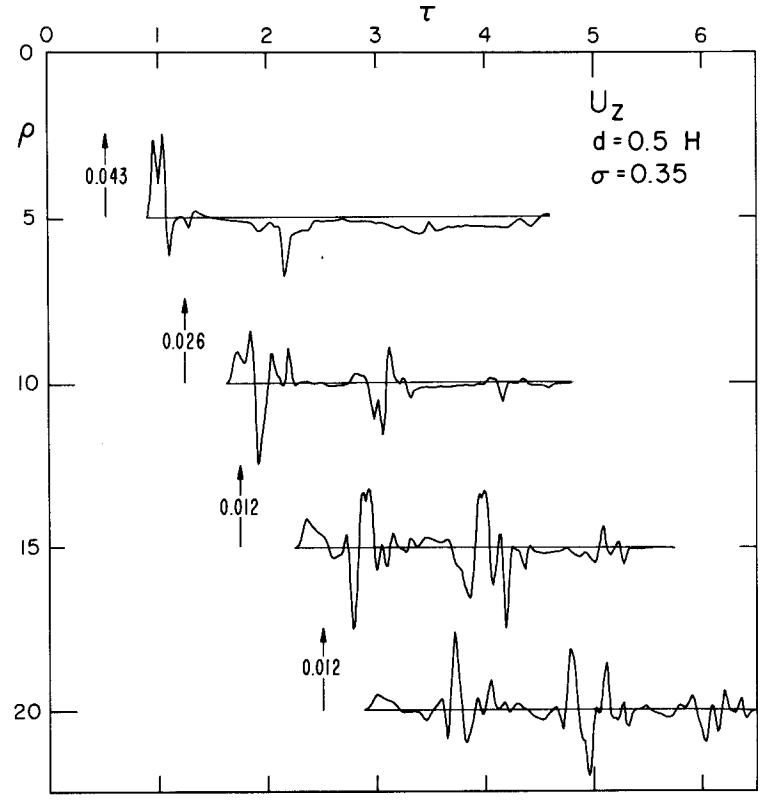

FIG. 8. Vertical displacement for a soft layer over a solid half-space.

1971). Applying a low-pass filter to such a response tends to average out the peaks. The results are that long-period waves are not affected much by the surface layers. The same conclusion is reached by Dainty (1971) based on "leaking mode" studies. As for the bottom boundary condition, the crust-mantle transition is probably not an interface. However, the refracted ray along the top of the mantle is not particularly influenced by a transition zone, except to shift the position of the critical angle (see Fuchs, 1969). Then, since we suppose that most of the long-period response is controlled by refractions, the simple interface approximation has some validity.

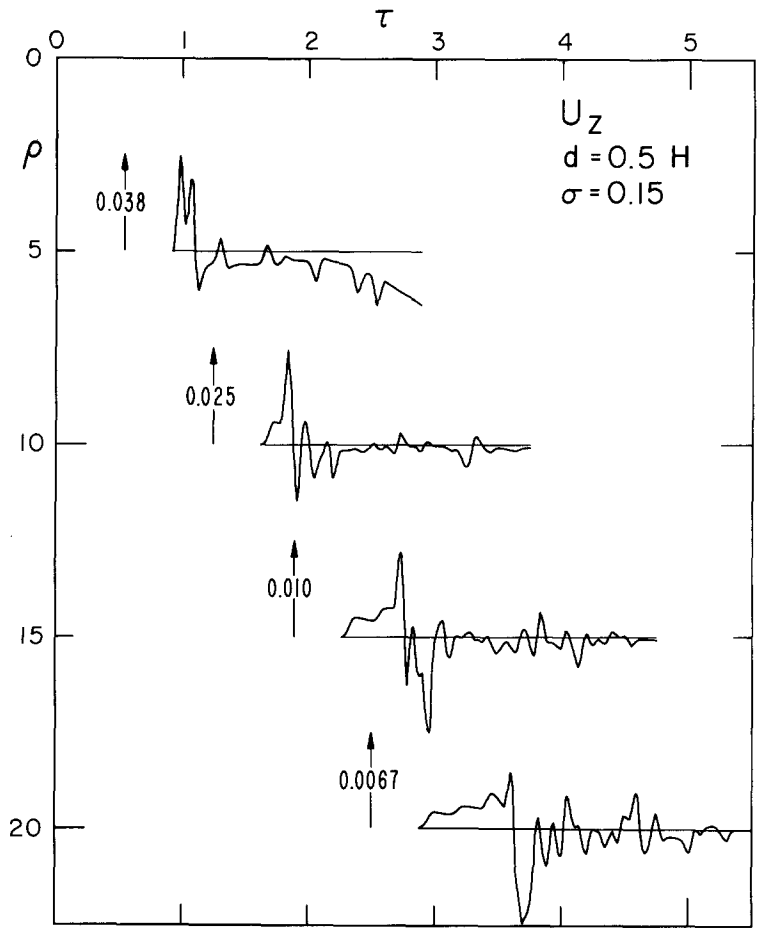

FIG. 9. Vertical displacement for a hard layer over a solid half-space.

We used the Hagiwara (1958) instrument-response curve appropriate for the Geotech *LP* with natural periods $T_s = 20$ secs, $T_g = 30$ secs, and damping factors $\lambda_s = 0.625$, $\lambda_g = 1$, and $\sigma^2 = 0.004$. We assumed the point-source pressure history to have the following form

$$s(t) = t\, e^{-\sigma t}$$

with $\phi = 0.25$. If the crustal model produces no propagational distortions, then the synthetic seismogram for the vertical displacement at the surface with the above assumptions would look like the *solid curve* in Figure 12.

We considered two models having the same crustal parameters but different mantle structures. The crustal layer parameters are assumed to be $C_1 = 6.15$ km/sec, $S_1 = 3.55$ km/sec and $D_1 = 2.74$ gm/cm^3. The layer is 40 km thick with the point source situated 4 km from the surface. As mentioned earlier, we assume that the *PL* wave is generated by only a layer over a half-space. Thus, for complicated models such as models I and II displayed in Figure 13, we assume in a preliminary calculation that the

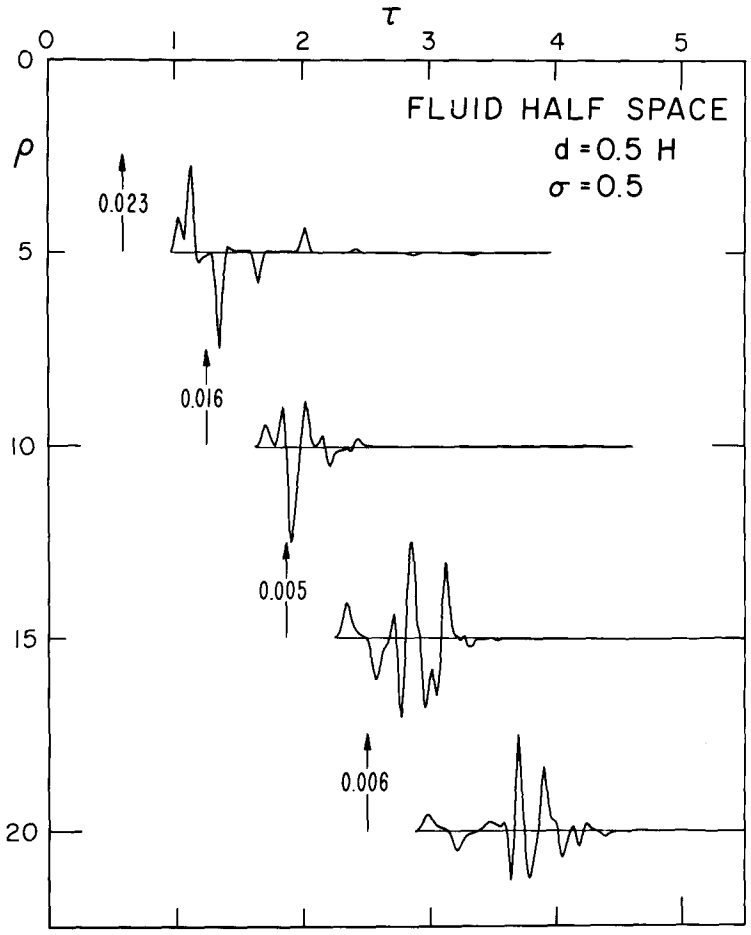

FIG. 10. Vertical displacement for a fluid layer over a fluid half-space.

mantle is homogeneous with the half-space parameters defined at the top of the mantle, referred to as crustal model I and II. The parameters assumed are $C_2 = 8.14$, $S_2 = 4.7$ and $D_2 = 3.3$ for model I and $C_2 = 7.85$, $S_2 = 4.5$ and $D_2 = 3.3$ for model II. The densities and shear velocities for the upper-mantle models approximate the Birch model. A plot of model *R* by Johnson (1967) is included in Figure 13 for comparison. The synthetic seismograms generated for crustal model I are given in Figure 14 (see column A). The refracted *PP* ray dominates the first arrival as documented earlier, whereas the *PL* wave is made up of many rays involving at least one *S*. That is, *PL* at large Δ is the combination of many reflected-refracted rays that spend most of their travel paths as spherical waves in the crust. Thus the *PL* wave is much less influenced by the low-velocity zone, LVZ, than is the *P* wave.

To test the dependence of the *P* wave on the LVZ, we included the appropriate generalized rays based on model I, Figure 13. The results are given in column B in Figure 14, where we have neglected mixed-mode generalized ray paths that would modify the *PL* wave somewhat. As the lid above the LVZ becomes thin, the effect on the *PL* wave becomes severe and should be investigated. In Figure 15 and Figure 16, we show the effects of the various generalized rays on the production of the *P* wave assuming model II.

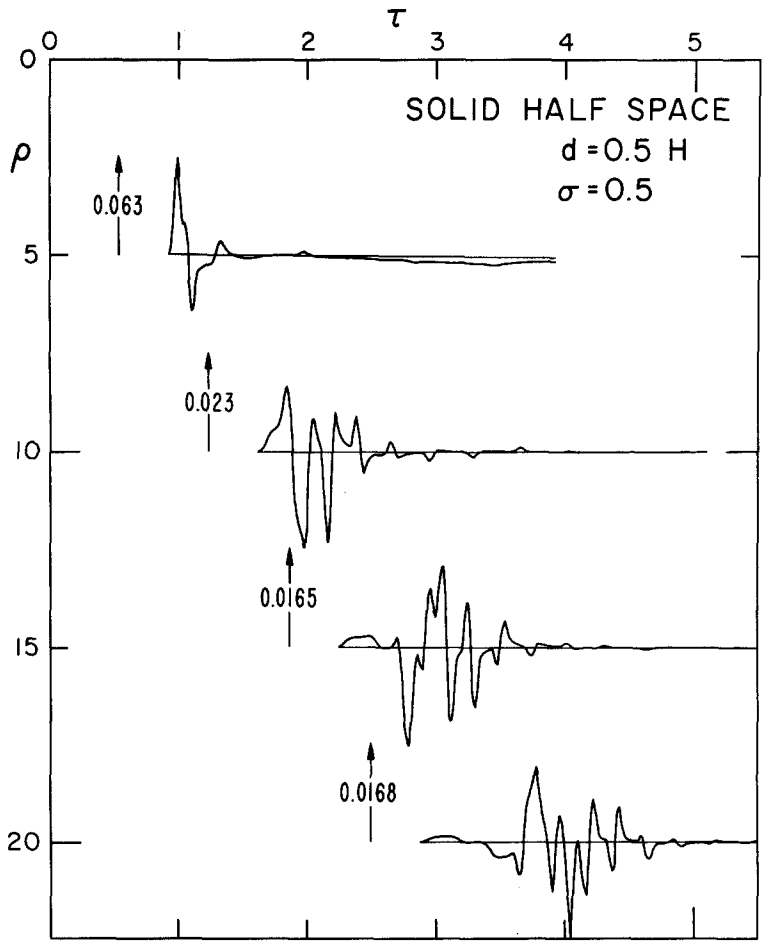

FIG. 11. Vertical displacement for a fluid layer over a solid half-space.

Column A of Figure 15 is just the crustal model response; column B includes the generalized rays representing the low-velocity gradient. Putting in the gradient has the effect of slowing down the *P* wave. In Figure 16, column A, we included the remaining rays. The bottom of the LVZ puts the *P* wave back in the synthetics with emphasis on the shorter periods. Applying a *Q*-operator (see Carpenter, 1967) to those rays returning from below the LVZ produces column B. We assumed $Q = 200$, $T_{au} = 1000/8$ and applied the operator at all ranges. Thus the seismograms at shorter ranges have an effective *Q* of about 100.

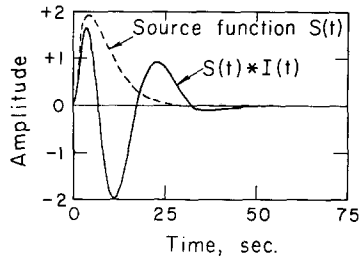

FIG. 12. Source function and interaction with the instrumentation; amplitude is in arbitrary units.

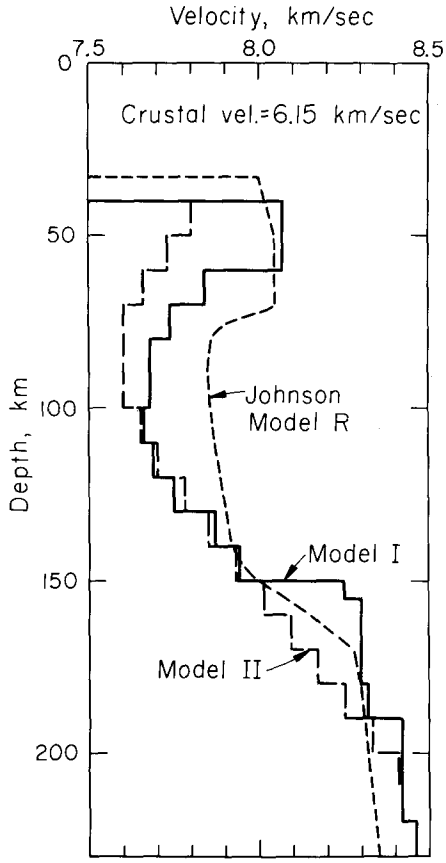

FIG. 13. Compressional velocity models of the LVZ.

Discussion

In this section, we will compare the synthetic seismograms generated from the two models with observations. An interpretation of the observations is given with respect to the LVZ and possible Q structure. A measure of the relative time delay between P and PL is defined and a reconnaissance map of lateral variations is presented.

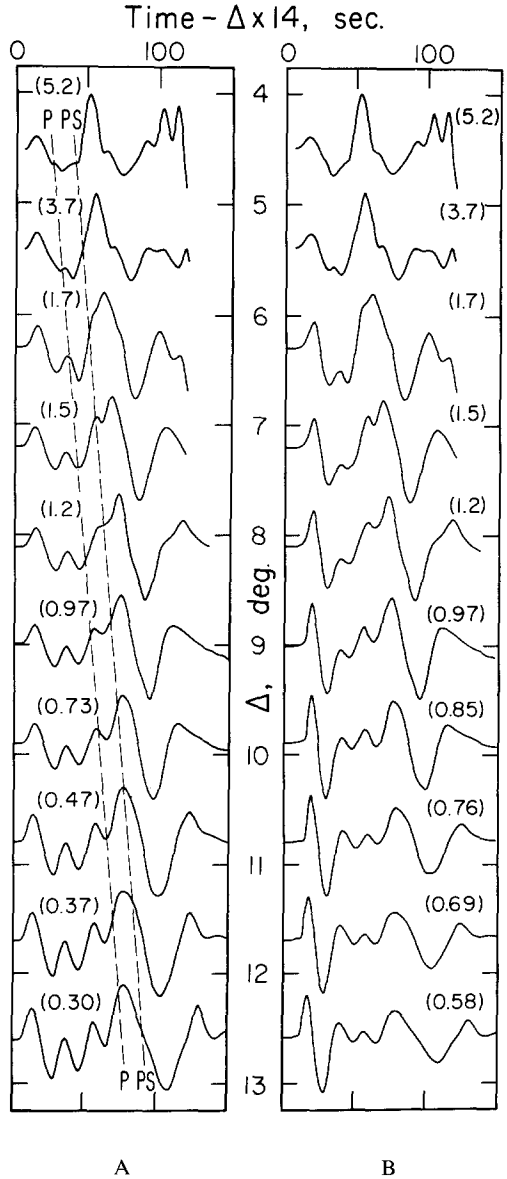

FIG. 14. Synthetic seismograms: column A for a layer over a half-space, and column B for model I. The direct P and reflected PS times are indicated. The numbers above the various recordings indicate the maximum amplitude of that trace.

The amplitude ratio of the synthetic PL waves between 7 to 13° is about 5. The corresponding decay of the observed PL is about the same (see Figures 1 and 14). The dominant period of the synthetic as well as the observed PL waves varies from 30 to 50 secs over this range. A comparison at 9° is given in Figure 17. The first peak and trough

of the *PL* wave are in reasonable agreement. The synthetic second peak is somewhat smaller than the corresponding observed.

It is interesting to compare this earthquake with the NTS event BOXCAR at 9° (see Figure 18). These events have about the same M_b magnitude of 6. However, the ampli-

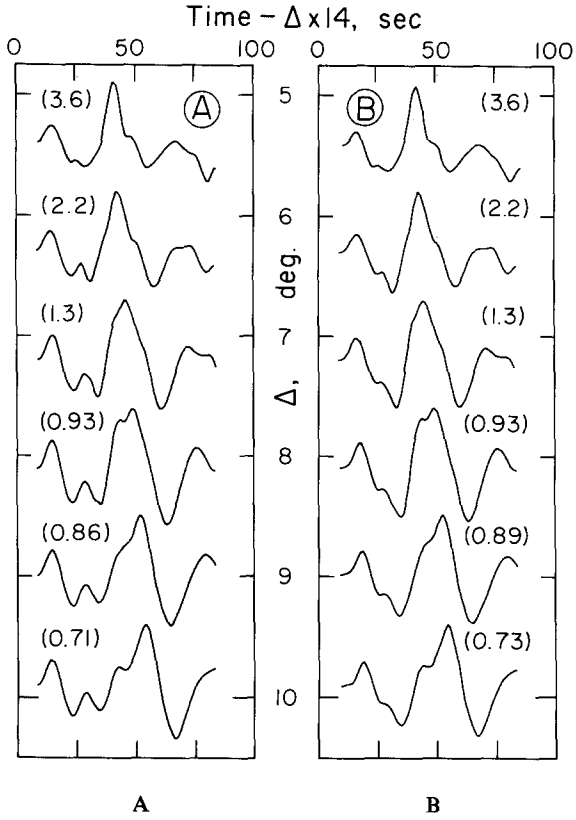

FIG. 15. Synthetic seismograms: column A is appropriate for a layer over a half-space, and column B contains the low-velocity gradient effects as well.

fication of *LC* is about 10 times greater than *JU* which is in agreement with recent spectral studies. The vertical component leads the radial slightly but this may not be significant. The model studies by Abramovici (1970) do not indicate any appreciable phase shift at these ranges. The ratio of *PL* to *P* is larger on the radial component than on the vertical as expected. This feature is observed on most of the recordings used in this study.

We will now return to model I and discuss alterations that are needed to explain the data. The synthetic seismogram at 12.6° compares favorably with GVTX with respect to the amplitude ratio of *P* to *PL* as well as in travel times. This feature is strong evidence for a prominent LVZ. At smaller ranges, for example JUTX, the synthetic *P* wave is too large and also contains too high a frequency. The interpretation is that for ranges less than 10°, the "*Q*" effect suppresses the *P* wave. That is, at these ranges, the generalized rays are bottoming at the base of the LVZ, and, since they travel the farthest in the absorbing zone, the effect is the most severe. At larger ranges, the rays bottom below this zone and are less affected.

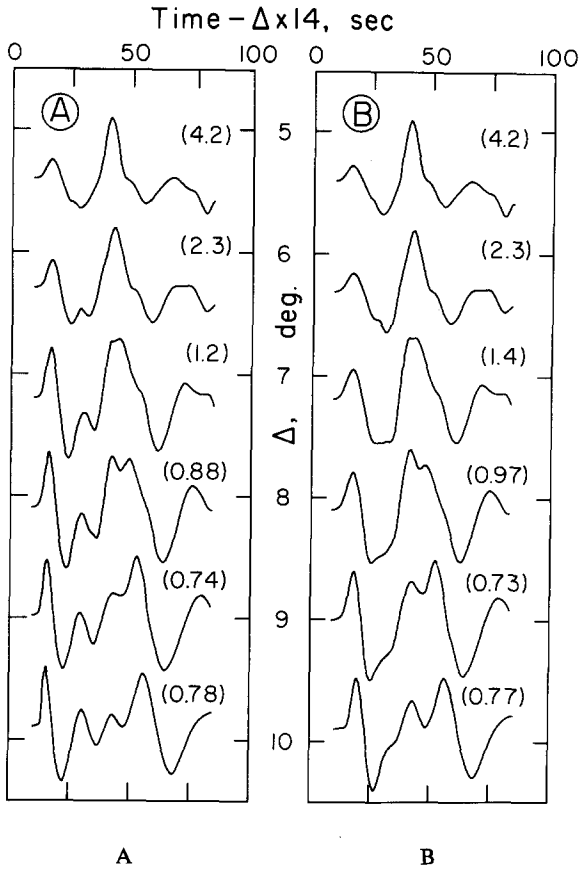

FIG. 16. Synthetic seismograms: column A is based on model II and column B displays the effect of an absorption operator applied to column A.

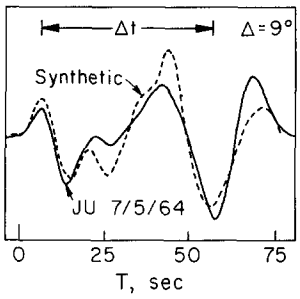

FIG. 17. Comparison of the synthetic trace, $\Delta = 9°$, column A, Figure 15, with the JU observations of the July 5, 1964 event.

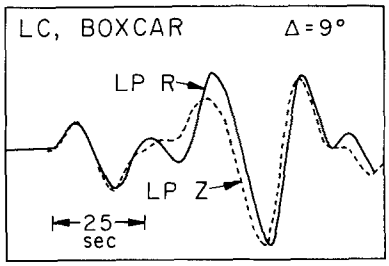

FIG. 18. Superposition of the vertical and radial displacement recordings of the BOXCAR event.

It appears that the same basic model can be used to explain the profile running through EKNV. The simplest alteration is to bring the top of the LVZ upward. This feature would explain the slowing down of the *P* wave as discussed earlier. For example, the synthetics in columns B, Figures 15 and 16, look much like SNAZ and SGAZ. The *PL* wave at WOAZ, not shown, is also somewhat late. This effect would be expected if the lid becomes too thin. Reducing the thickness of the lid would also explain the delay time observed at EKNV and stations along this profile.

Finally, we introduce a rather simple criterion for use in mapping lateral variations. In Figure 17, we defined a Δt which is a measure of the separation of *P* from *PL*. That is, we measure the time from the first peak of the *P* wave to the first trough of the *PL*. A plot of Δt versus range for a number of events is given in Figure 19. The line indicates the

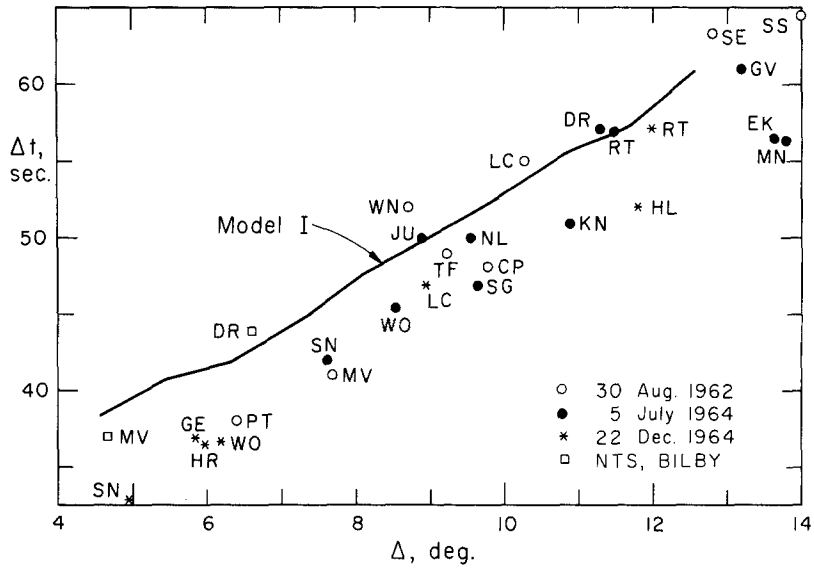

FIG. 19. Lateral variations using the Δt measure; locations are given in Figure 2.

Δt measure applied to the synthetics. The separation is the largest in profiles running from the Utah–Idaho event toward the Midwest. The smallest Δt's occur between Baja, California and Idaho. There is a large amount of data in Figure 19 since the profiles are interlaced. A partial path type of approach is required to delineate the zone of highest delay. However, the eastern boundary is fairly obvious. A line running from *HL* to *NL* appears to be the eastern limit (see *LC* from the Utah–Idaho event and *NL* from the Gulf of California). The zone must be quite narrow as inferred from profiles crossing at

various angles. Actually, Figure 19 is only useful as a reconnaissance tool since the *PL*-wave velocity does vary as mentioned earlier. This means that the travel times of both *P* and *PL* should be used in the delineating process. This approach will be followed in a later paper.

Conclusions

The model of a solid layer over a solid half-space appears to explain many features of long-period *PL*-wave propagation from 4 to 13°. The amplitude decay as well as the dispersive properties of the synthetic seismograms are in good agreement with the LRSM observations. Model studies indicate that the *PL* wave is not very sensitive to focal depth except that the source is located in the layer. This means that the long-period *PL* wave is not very exciting as a seismic exploration tool but makes an excellent standard with respect to amplitude and arrival time. Since radial profiles of long-period data are difficult to obtain, one can use the *PL* waves as a measure of source function intensity at least for simple fault orientations, for example, double-couple strike-slip fault. The problem of a double couple with arbitrary orientation will be considered in a later paper.

The long-period *P* wave is much more interesting at these ranges since it samples the velocity structure far below the crust. The observations indicate that *PL* is larger than *P* for ranges less than about 10° where a crossover in amplitude occurs. This feature is explained by the presence of a LVZ. The bottom of the LVZ provides the structure needed to increase the amplitude of *P* at the largest ranges. The negative gradient at the top of the mantle plus the absorption effects of a major LVZ explains the absence of the early arriving P_n in some profiles, the profile running from the Gulf of California to Nevada being the best example.

We have not explored the uniqueness of our model in this study but have concentrated on exploring the lateral variation that the data suggest. A simple measure of observed lateral variation is the separation between the *P* and *PL* arrivals. This criterion was used to delineate the abnormal LVZ in Western United States.

The observations used in this study are only a small sample of the LRSM data available on this subject. These data are being collected. However, since we are dealing with a frequency-dependent problem, it becomes increasingly clear that broad-band seismic information is required. These types of data will be available in the near future, at which time an attack on the fine structure of the LVZ will be in order.

Acknowledgments

I thank Drs. Freeman Gilbert and David Harkrider for their advice and constructive criticism.

This research was supported by the Air Force Office of Scientific Research, under Contract AFOSR (F44620-69-C-0067).

References

Abramovici, F. (1970). Numerical seismograms for a layered elastic solid, *Bull. Seism. Soc. Am.* **60,** 1861–1876.

Barker, T. (1970). Response of an elastic layer over an elastic half space to a point source, *Master's Thesis,* Massachusetts Institute of Technology.

Carpenter, E. W. (1967). Teleseismic signals calculated for underground, underwater, and atmospheric explosions, *Geophysics* **32,** 17–32.

Dainty, A. M. (1971). Leaking modes in a crust with a surface layer, *Bull. Seism. Soc. Am.* **61,** 93–107.

Fuchs, K. (1969). Reflection of spherical waves from transition zones with arbitrary depth-dependent elastic moduli and density, *J. Phys. Earth* **16,** 27–41.

Gilbert, F. (1964). Propagation of transient leaking modes in a stratified elastic waveguide, *Rev. Geophys.* **2,** 123–153.

Gilbert, F. and D. V. Helmberger (1971). Generalized ray theory for a layered sphere, *Geophys. J.* (in press).

Gilbert, F. and S. J. Laster (1962). Excitation and propagation of pulses on an interface, *Bull. Seism. Soc. Am.* **52,** 299–319.

Hagiwara, T. (1958). A note on the theory of the electro-magnetic seismograph, *Bull. Earthquake Res. Inst., Tokyo Univ.* **36,** 139–164.

Helmberger, D. (1968). The crust-mantle transition in the Bering Sea, *Bull. Seism. Soc. Am.* **58,** 179–214.

Johnson, L. R. (1967). Array measurements of *P* velocities in the upper mantle, *J. Geophys. Res.* **72,** 6309–6325.

Oliver, J. and M. Major (1960). Leaking modes and the *PL* phase, *Bull. Seism. Soc. Am.* **50,** 165–180.

Pekeris, C. L. (1948). Theory of propagation of explosive sound in shallow water, *Geol. Soc. Am., Mem. 27.*

Pekeris, C. L., I. M. Longman, and H. Lifson (1959). Application of ray theory to the problem of long-range propagation of explosive sound in a layered liquid, *Bull. Seism. Soc. Am.* **49,** 274–250.

Pekeris, C. L., Z. Alterman, F. Abramovici, and H. Jarosch (1965). Propagation of a compressional pulse in a layered solid, *Rev. Geophys.* **3,** 25–47.

Phinney, R. A. (1961a). Leaking modes in a crustal waveguide. Part I: The oceanic *PL* wave, *J. Geophys. Res.* **66,** 1445–1470.

Phinney, R. A. (1961b). Propagation of leaking interface waves, *Bull. Seism. Soc. Am.* **51,** 527–555.

Rosenbaum, J. H. (1960). The long-time response of a layered elastic medium to explosive sound, *J. Geophys. Res.* **65,** 1577–1614.

Strick, E. (1959). Propagation of elastic wave motion from an impulsive source along a fluid-solid interface Parts II and III, *Phil. Trans. Roy. Soc. London, Ser. A,* **251,** 465–523.

Su, S. S. and J. Dorman (1965). The use of leaking modes in seismogram interpretation and in studies of crust-mantle structure, *Bull. Seism. Soc. Am.* **55,** 989–1021.

Sykes, L. R. (1970). Focal mechanism solutions for earthquakes along the world rift system, *Bull. Seism. Soc. Am.* **60,** 1749–1752.

SEISMOLOGICAL LABORATORY
CALIFORNIA INSTITUTE OF TECHNOLOGY
PASADENA, CALIFORNIA
DIVISION OF GEOLOGICAL SCIENCES
CONTRIBUTION NO. 2045

Manuscript received July 14, 1971